# Effects of laser surface melting on crystallographic texture, microstructure, elastic modulus and hardness of Ti−30Nb−4Sn alloy

Leonardo FANTON[1], Nelson Batista de LIMA[2], Emilio Rayón ENCINAS[3],
Vicente Amigó BORRÁS[3], Conrado Ramos Moreira AFONSO[4], João Batista FOGAGNOLO[1]

1. School of Mechanical Engineering, University of Campinas,
Rua Mendeleyev, 200, CEP 13083-860, Campinas, SP, Brazil;
2. Instituto de Pesquisas Energéticas e Nucleares, Av. Prof. Lineu Prestes, 2242, CEP 05508-000, São Paulo, SP, Brazil;
3. Institut de Tecnologia de Materials, Universitat Politècnica de València,
Camino de Vera, s/n, Código Postal 46022, Valencia, Spain;
4. Department of Materials Engineering, Federal University of São Carlos,
Rodovia Washington Luís, Km 235, CEP 13565-905, São Carlos, SP, Brazil

**Abstract:** The biocompatibility of orthopedic implants is closely related to their elastic modulus and surface properties. The objective of this study was to determine the effects of cold rolling, recrystallization and laser surface melting (LSM) on the microstructure and mechanical properties of a biphase ($\alpha''+\beta$) Ti−30Nb−4Sn alloy. X-ray diffraction (XRD) texture analysis of the cold-rolled substrate revealed the $[302]_{\alpha''}$//ND texture component, while analysis of the recrystallized substrate showed the $[302]_{\alpha''}$//ND and $[110]_{\alpha''}$//ND components. The $\beta$-phase texture could not be directly measured by XRD, but the presence of the $[111]_{\beta}$//ND texture component was successfully predicted by considering the orientation relationship between the $\alpha''$ and $\beta$ phases. Nanoindentation measurements showed that the elastic modulus of the cold-rolled substrate (63 GPa) was lower than that of the recrystallized substrate (74 GPa). Based on the available literature and the results presented here, it is suggested that this difference is caused by the introduction of crystal defects during cold deformation. The combined nanoindentation/EBSD analysis showed that the nanoindentation results are not affected by crystal orientation. LSM of the deformed alloy produced changes in hardness, elastic modulus and crystallographic texture similar to those produced by recrystallization heat treatment, creating a stiffness gradient between surface and substrate.

**Key words:** titanium alloy; cold rolling; laser surface melting; recrystallization; crystallographic texture; stiffness-graded material

## 1 Introduction

Titanium and its alloys have high corrosion resistance in aqueous media, high specific strength and low elastic modulus, making them attractive for many applications. Because of its good biocompatibility and relatively low elastic modulus, titanium is one of the preferred materials for use in the manufacture of medical implants to replace hard tissues. Among the most common metal alloys used to produce implants, $\beta$-type titanium alloys possess the lowest elastic modulus (about 60 GPa) [1]. However, this value is still at least twice the stiffness of bone [2], and the load is therefore not properly transferred between the bone and implant. Because of this phenomenon, known as the stress shielding effect [3], the bone receives insufficient mechanical stimulus and may therefore become less dense. On the other hand, implants with a low

elastic modulus have been identified as the cause of micromotion at the interface between the bone and implant, leading to the growth of fibrous tissues and potentially causing premature failure [4,5]. Although stress shielding and interface micro-motion are issues that require conflicting solutions, finite element simulations have shown that in the case of femoral hip implants a good compromise can be achieved by having variable stiffness and a higher elastic modulus in the proximal region [6]. A stiffness gradient allows optimized load transfer between implant and bone, minimizing both stress shielding and interface micromotion [4].

Despite good biocompatibility of titanium, the problem of implant rejection has to be completely solved. In addition, titanium is known to have poor wear performance [7] because of its high friction coefficient. As biocompatibility and wear resistance are properties related to the surface of a material, a number of surface modifications have been proposed for titanium alloys [8]. BALLA et al [9] found that laser surface melting (LSM) provides improved wear and corrosion resistances for Ti−6Al−4V alloys. LSM can also improve biocompatibility by creating a surface roughness that favors cell adhesion and is less time-consuming and cleaner than other surface texturing techniques such as chemical etching and anodization, as pointed out by PRODANOV et al [10].

The control of the preferred orientation of grains (crystallographic texture) is a recognized approach for enhancing the properties of metal alloys. The crystallographic texture of a material depends on its processing route and can be modified by four main processes: (i) solidification, (ii) hot or cold working, (iii) recrystallization and (iv) phase transformation [11]. It has been shown that crystallographic texture can be an important factor affecting surface-related properties of titanium alloys such as wettability, corrosion resistance and biocompatibility [12]. Because the surface energy of lattice planes depends on the atomic density, the surface properties of these alloys depend on the particular plane that is exposed on the surface [13]. Texture also induces anisotropy of mechanical properties, such as strength and elastic modulus [14].

Like other Ti−Nb alloys [15,16], Ti−30Nb−4Sn alloy has low elastic modulus (60−80 GPa) [17] and contains no toxic elements, making it a good

candidate for using in the production of orthopedic implants. When the alloy is quenched from temperatures above the $\beta$-transus, the $\beta$ phase partially transforms to the $\alpha''$ phase by a martensitic (diffusionless) phase transition. The final micro-structure of the alloy is composed of a matrix of $\beta$ (body-centered cubic crystal lattice) grains enclosing $\alpha''$ (orthorhombic crystal lattice) plates [18]. Although the $\beta \rightarrow \alpha''$ phase trans-formation can also be strain-induced [19] during cold rolling, it is not clear if this transformation can cause significant changes to the elastic modulus. Some studies suggest that the increase in $\alpha''$ content could reduce the elastic modulus [20,21]. However, the study of LEE et al [22] on Ti−Nb alloys with different Nb contents demonstrated that the bending modulus of an alloy composed mostly of $\alpha''$ phase (Ti−20Nb) was close to that of a full-$\beta$ alloy (Ti−35Nb).

Various systematic studies on the development of rolling texture in $\beta$ [23] and $\alpha$ (hexagonal crystal lattice) titanium alloys [24−26], and studies on the texture of multiphase titanium alloys, such as the traditional Ti−6Al−4V ($\alpha+\beta$) alloy [27], intermetallic Ti−Al alloys [28] and Ti−Ni composite materials [29] can be found in the literature. For $\alpha''+\beta$ titanium alloys, however, less information is available. To the best of our knowledge, there are no studies on the recrystallization texture of $\alpha''+\beta$ titanium alloys. This study aims to investigate the effects of both recrystallization and LSM on the microstructure, crystallographic texture, hardness and elastic modulus of highly deformed Ti−30Nb−4Sn alloy.

## 2 Experimental

The Ti−30Nb−4Sn alloy used here was produced in an electric arc furnace with an argon atmosphere, homogenized at 1000 °C for 8 h and water quenched. The composition of the alloy, which was measured by X-ray fluorescence spectroscopy (XRF) (Shimadzu EDX 7000 spectrometer), was 29.2 wt.% Nb and 3.9 wt.% Sn and balance Ti. Oxygen and nitrogen contamination, which were determined with a LECO (model TC400) analyzer, were 0.13 wt.% and 0.0045 wt.%, respectively. The ingot was cold-rolled (at room temperature) until an 85% reduction in thickness was achieved. Part of the rolled sample was heat-

treated at 800 °C (above the $\beta$-transus) for 30 min to promote recrystallization and then quenched in water. The alloys in the as-deformed state and after recrystallization (and quenching) will henceforth be referred to as the deformed and recrystallized alloys, respectively. The duration of the recrystallization heat treatment was chosen based on our experience with similar alloys [18]. To prevent oxidation during the homogenization and recrystallization treatments, the specimens were encapsulated in a quartz tube filled with high-purity argon (99.999%). For the water quenching, the quartz tube was removed from the furnace and immediately broken so that the sample fell into a container with water. As usual for rolled specimens, the external reference frame for the deformed and recrystallized alloys is the normal direction (ND) (orthogonal to the rolling surface), rolling direction (RD) and transverse direction (TD).

The rolling surfaces of the deformed and recrystallized alloys were laser-melted by over-lapping multiple laser-tracks orthogonal to the RD. An ytterbium fiber laser source with a wavelength of 1070 nm and a Gaussian beam was used. The process was carried out inside a glovebox filled with argon gas (99.999%) to avoid oxidation. The distance between the center of one laser track and the next was 175 μm, and the sample was moved at a speed of 600 mm/min relative to the laser source. The laser power was 150 W, and the beam was focused on the surface of the sample.

For the microscopy analyses, the specimens were prepared by grinding with SiC abrasive paper up to 1200 grit, followed by polishing with diamond paste (9 μm) and finally polishing with colloidal silica suspension (0.05 μm). Visible-light microscopy (VLM) was performed with a reflected light differential interference contrast (DIC) microscope using Kroll's etchant to reveal the microstructure. The EBSD analysis was carried out on a ZEISS (AURIGA Compact) electron micro-scope equipped with a field-emission electron gun and an OXFORD EBSD system using AZtecHKL data-acquisition software.

A G−200 nanoindenter from Agilent Technology (Santa Clara, USA) was used to determine the hardness and elastic modulus (Young's modulus). Measurements were made as a function of the depth of penetration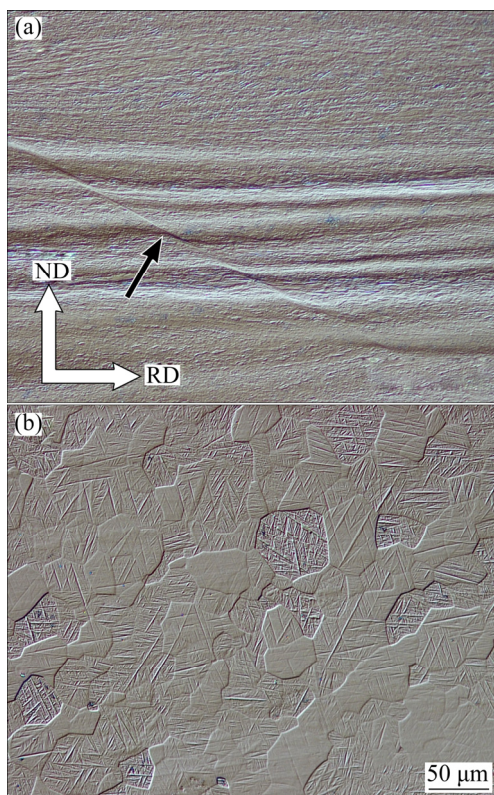 using the continuous stiffness measurement (CSM) method [30]. A constant maximum depth of 1500 nm was used, and only measurements between 1000 and 1500 nm were considered to calculate the average. A Berkovich-geometry tip was used, and the indenter shape was calibrated previously by indenting a sample of fused silica with a known elastic modulus. The elastic modulus was calculated from the reduced modulus using a Poisson ratio of 0.42 obtained from ultrasound (pulse-echo) measurements.

The experimental pole figures used to evaluate the crystallographic texture were determined by XRD with a Panalytical X'Pert Pro diffractometer. Orientation distribution functions (ODFs) were calculated from the pole figures with the MTEX toolbox for MATLAB$^{TM}$ [31]. The pole figure inversion method used by MTEX to generate the ODFs has been explained in detail by HIELSCHER and SCHAEBEN [32]. Only the texture of the $\alpha''$ phase could be determined by XRD because the $\beta$-phase peaks overlapped with $\alpha''$ peaks and could not be clearly distinguished in the XRD patterns. The 022, 110, 112, 113, 130, 131 and 200 pole figures were measured and used to calculate the ODF of each sample. Although it was not measured experimentally, the $\beta$-phase texture was predicted for the recrystallized alloy based on the orientation relationship (OR) between the $\alpha''$ and $\beta$ phases. For the deformed alloy, such a prediction cannot be used since the textures of the $\alpha''$ and $\beta$ phases may have evolved differently during cold rolling, as a result of which the OR may not apply. The parent ($\beta$) and product ($\alpha''$) phases must obey the following ORs: $(100)_\beta//(100)_{\alpha''}$ and $[011]_\beta//[010]_{\alpha''}$ [33]. In other words, the texture of the $\alpha''$ phase is a transformation-type texture inherited from the texture of the $\beta$ phase. For the $\beta \rightarrow \alpha''$ phase transformation, each given orientation of the parent $\beta$ phase (considering all symmetrically equivalent orientations) can generate six different orientations of $\alpha''$ (six variants). For the reverse transformation ($\alpha'' \rightarrow \beta$), only one (unique) orientation of the parent $\beta$ phase is possible for any of the six variants [34]. Consequently, the orientation of the parent phase can be determined given the orientation of any of the variants. The MTEX toolbox [31] was used to calculate the ODF of the $\beta$ phase based on the ODF of the $\alpha''$ phase previously calculated with experimental pole figures. The procedure used can be found on the MTEX Web page [35].

# 3 Results and discussion

## 3.1 Microstructure and crystallographic texture

The microstructures observed by VLM of the alloy in the deformed and recrystallized conditions are presented in Fig. 1. Grain boundaries were not visible in the microstructure of the deformed alloy (Fig. 1(a)) because of grain refinement. Some regions showed a wave-like pattern caused by deformation heterogeneities. Regions with a higher deformation became harder, and the amount of material removed during sample preparation (grinding and polishing) was therefore not homogeneous. Shear bands could also be observed, as indicated by an arrow in Fig. 1(a). The recrystallized alloy (Fig. 1(b)) exhibited well-defined equiaxed grains with an average grain size of approximately 30 μm, and the martensite laths were clearly visible inside the grains. The relatively homogenous grain-size distribution indicates that recrystallization was complete. As reported by SALVADOR et al [18], Ti−30Nb−4Sn alloy has a microstructure composed of a matrix of $\beta$ phase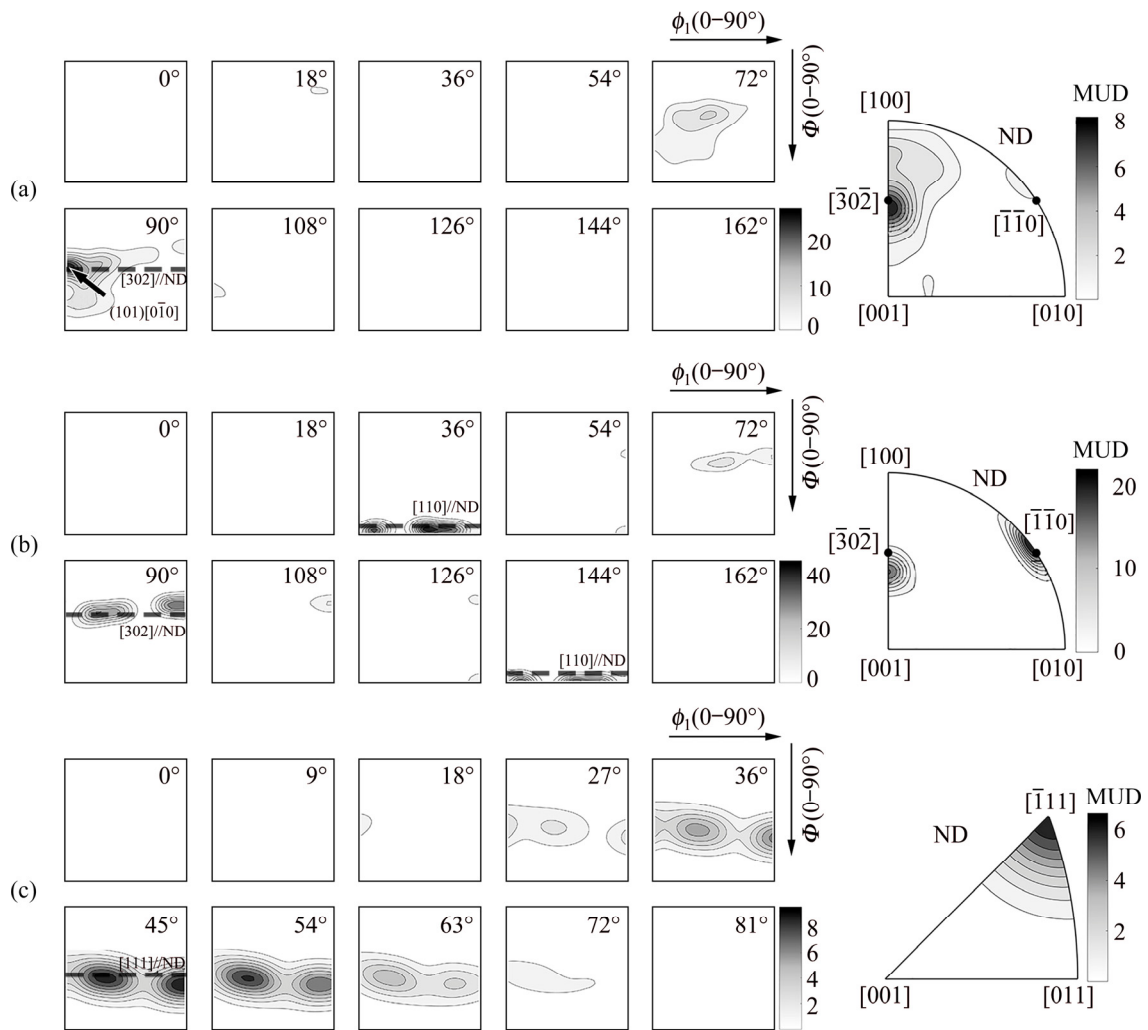 with $\alpha''$ plates after quenching from temperatures above the $\beta$-transus. Hence, the recrystallized grains should correspond to the $\beta$-phase grains prior to quenching and the martensite plates to the $\alpha''$ phase that formed during cooling.

The $\alpha''$ ODFs for the deformed and the recrystallized alloys and the $\beta$ ODF predicted for the recrystallized alloy are displayed in Fig. 2. The latter was predicted based on the OR between the $\alpha''$ and $\beta$ phases, as previously indicated. The inverse pole figures (IPFs) showing the crystal directions aligned to the ND could be seen to the right of each ODF. The intensity of the ODFs and IPFs was given by multiples of uniform density (MUD), also called multiples of random distribution (MRD), and represents how many times a certain orientation is more textured than it would be in a material with a uniform distribution of orientations (i.e., an untextured material). The IPFs allow the crystallographic texture components to be visualized more easily but do not allow a peak-type texture component to be distinguished from a fiber-texture one. Dashed lines in the ODFs indicated the ideal position of the fiber components. The ODF of the deformed alloy ($\alpha''$ phase) (Fig. 2(a)) showed only one main texture component, $(101)[0\bar{1}0]_{\alpha''}$, which could also be considered part of an incomplete fiber texture, $[302]_{\alpha''}//\text{ND}$. Recrystallization increased the intensity of the $[302]_{\alpha''}//\text{ND}$ fiber texture (Comparing the texture intensities in the ODFs and IPFs (Figs. 2(a, b))), and a new fiber texture component, $[110]_{\alpha''}//\text{ND}$, appeared; this was as strong as the $[302]_{\alpha''}//\text{ND}$ component. The $\beta$-phase texture predicted for the recrystallized alloy (Fig. 2(c)) showed the $[111]_{\beta}//\text{ND}$ texture component.

EBSD analysis of a random region of the recrystallized alloy was carried out. Figure 3 shows the band contrast (Kikuchi pattern quality) map for this region and the IPFs of $\alpha''$ and $\beta$ phases with the crystal orientations aligned to the ND. The similarity of the IPFs in Fig. 3 with the IPFs for the $\alpha''$ and $\beta$ phases in Figs. 2(b) and (c) indicates that the result of the EBSD is in accordance with the $\alpha''$ texture measured experimentally by XRD and the $\beta$ texture predicted theoretically. The EBSD technique could not be used to analyze the deformed alloy as Kikuchi patterns produced by highly deformed materials tend to be of poor quality due to resolution limitation associated with the fact that



**Fig. 1** VLM images of Ti−30Nb−4Sn alloy in deformed (a) and recrystallized (b) conditions (Black arrow in (a) indicates shear band)

**Fig. 2** ODFs of $\alpha''$ phase in deformed (a) and recrystallized (b) alloys calculated from XRD data and ODF of $\beta$ phase for recrystallized alloy estimated theoretically (c) (Corresponding IPFs showing crystal directions aligned to ND are on right of each ODF. Scale bars represent multiples of uniform density (MUD))
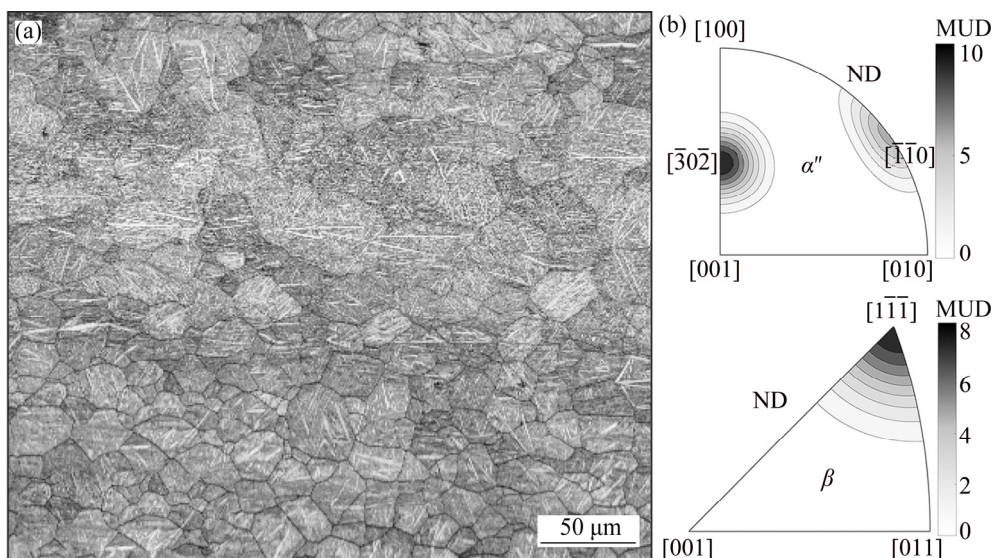


**Fig. 3** EBSD band contrast map for recrystallized alloy (a) and IPFs of $\alpha''$ and $\beta$ phases showing crystal orientations aligned to ND (b)

the size of the electron beam interaction volume is too large compared with the fine-scale micro-structure [36].

The cold-rolling texture components found in this study are different from those reported in the Refs. [37−40] for other $\alpha''+\beta$ titanium alloys. HAYAMA et al [37] found the $(121)[\bar{2}14]_{\alpha''}$ and $(142)[\bar{2}13]_{\alpha''}$ textures for a cold-rolled Ti−35Nb alloy. MATSUMOTO et al [38,39] studied the texture of cold-rolled Ti−30Nb−4Sn and Ti−35Nb−7.9Sn alloys and found the $(220)[001]_{\alpha''}$, $(200)[010]_{\alpha''}$, $(211)[110]_{\beta}$, $(100)[110]_{\beta}$ and $(110)[112]_{\beta}$ components. No other studies on the recrystallization texture of recrystallized $\alpha''+\beta$ alloys were identified in the literature that could be used for the purposes of comparison. However, the $[111]_{\beta}$//ND fiber (also known as $\gamma$ fiber) can be expected as it is commonly found in body-centered cubic metals after cold rolling and recrystallization [40]. Table 1 summarizes the main texture components of the Ti−30Nb−4Sn alloy in the deformed and recrystallized conditions.

**Table 1** Main texture components of Ti−30Nb−4Sn alloy in deformed and recrystallized conditions using XRD and EBSD

| Condition | Technique | Phase | Main texture component |
|---|---|---|---|
| Deformed | XRD | $\alpha''$ | $[302]_{\alpha''}$//ND |
| Recrystallized | XRD | $\alpha''$ | $[302]_{\alpha''}$//ND and $[110]_{\alpha''}$//ND |
| | Theoretical prediction using XRD and OR | $\beta$ | $[111]_{\beta}$//ND |
| | EBSD | $\alpha''$ | $[302]_{\alpha''}$//ND and $[110]_{\alpha''}$//ND |
| | | $\beta$ | $[111]_{\beta}$//ND |

As already explained in materials and methods, the $\beta \rightarrow \alpha''$ phase transformation can result in six different orientations (variants) of $\alpha''$ phase for each orientation of $\beta$ phase. To correlate the $\alpha''$ variants with the texture found in the recrystallized alloy, EBSD analysis of a single recrystallized grain was performed (Fig. 4(a)). This particular grain was intentionally chosen because it is oriented with the $\langle 111 \rangle_{\beta}$ direction approximately parallel to the ND and is therefore an example of a grain that contributes to the $[111]_{\beta}$//ND texture component. As expected, six different orientations (variants) of $\alpha''$ were found in this grain, and these were named V1,

V2, V3, V4, V5 and V6. The results show that the $[011]_{\beta}$ direction is parallel to the $[010]_{\alpha''}$ direction, and the $(100)_{\beta}$ plane is parallel to the $(100)_{\alpha''}$ plane, in accordance with the OR expected for the $\alpha''$ and $\beta$ phases (related planes and directions are positioned close to each other in the stereographic projection). The $\alpha''$ variants also explain how the $[111]_{\beta}$//ND texture component is related to the $[110]_{\alpha''}$//ND and $[302]_{\alpha''}$//ND components. Whenever a parent $\beta$ grain is oriented with the $[111]_{\beta}$ direction aligned to the ND, three of the $\alpha''$ variants (in this case V1, V3 and V5) will have the $[110]_{\alpha''}$ direction parallel to the ND, and in other three variants (V2, V4 and V6) the $[302]_{\alpha''}$ direction will be parallel to the ND (highlighted region in Fig. 4(b)).
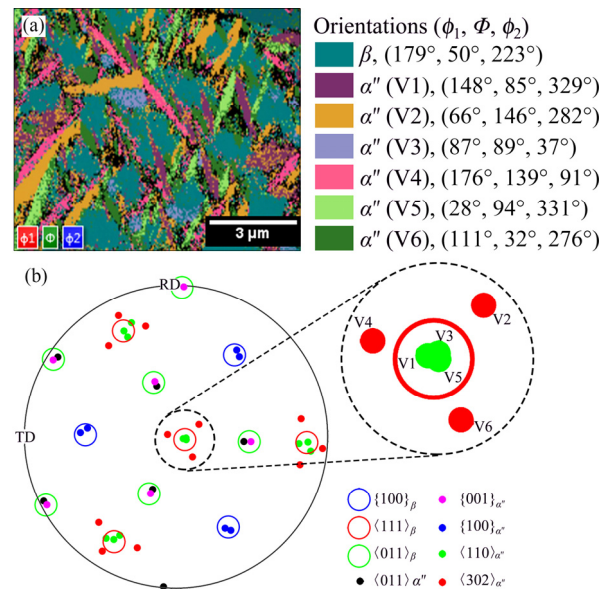


**Fig. 4** EBSD analysis of single grain composed of matrix of $\beta$ phase and $\alpha''$ martensite laths formed upon rapid cooling: (a) Colored Euler orientation map for $\beta$ and $\alpha''$ phases; (b) Pole figure plots for all identified orientations

**3.2 Laser surface melting**

Figure 5 shows the microscopy analysis of the deformed alloy after LSM treatment. The fusion zone (FZ) has a regular circular shape with an overlap of about 50% between two subsequent laser tracks (Fig. 5(a)). The FZ is immediately followed by the heat-affected zone (HAZ), which undergoes recrystallization and grain growth. Grain size decreases progressively as the distance from the FZ increases until the grains become so small that they can no longer be seen and the appearance of the alloy is the same as that of the substrate. The FZ can be divided into two regions according to the
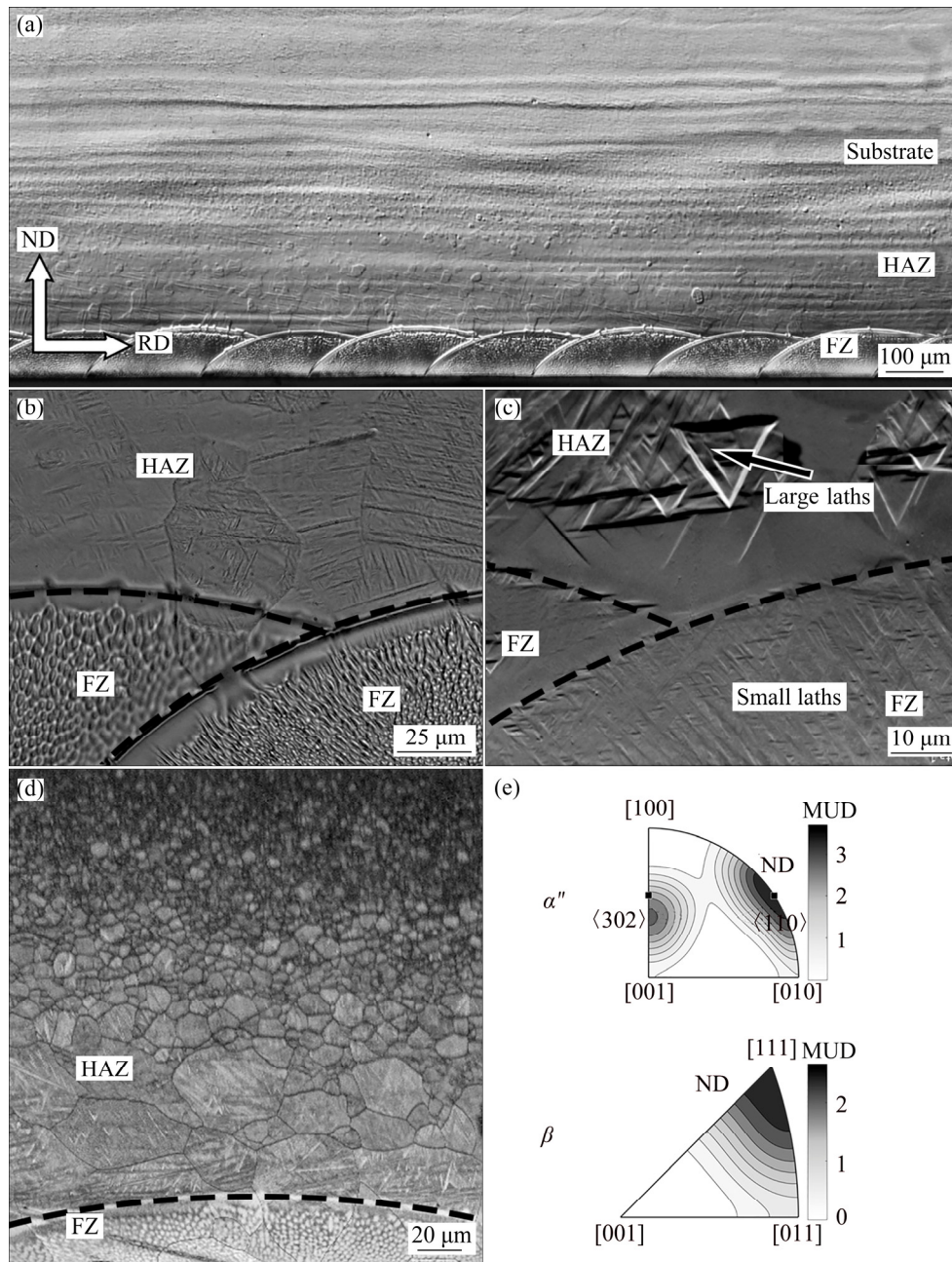
**Fig. 5** Microscopy analyses of deformed and laser-surface-melted sample (Dashed lines indicate FZ/HAZ interface): (a) VLM micrograph showing general view of FZ and HAZ; (b, c) VLM (b) and SEM (c) (forward scatter detector) images of highlighted FZ/HAZ interface; (d) EBSD band contrast map of FZ and HAZ; (e) IPFs of $\alpha''$ and $\beta$ phases

type of solidification growth. Near the FZ/HAZ interface, where solidification starts, there is a narrow band (Fig. 5(b)) approximately 10 μm in width in which solidification growth is planar. From that point on, the solidification growth in the FZ is cellular. This behavior can be explained by phenomenon known as constitutional undercooling [41]. Titanium is rejected during solidification, and the liquid close to the solidification front therefore becomes richer in this

element. This causes the liquidus temperature to change locally (constitutional undercooling), and when critical undercooling is achieved, the planar solidification front becomes unstable, giving rise to the cellular solidification growth observed here. Still in Fig. 5(b), a grain that extends over the boundary between the FZ and HAZ can be observed, indicating the epitaxial nature of the solidification process. The martensite ($\alpha''$) laths cannot be easily observed in the VLM micrographs

but can be clearly seen when SEM is used with a forward scatter detector (FSD) (Fig. 5(c)). Many martensite laths are arranged in a triangular fashion or delta distribution. The laths are significantly smaller in the FZ than those in the HAZ. The presence of the $\alpha''$ phase in the HAZ and FZ indicates that the cooling rate during LSM is sufficiently high to activate the martensitic $\beta \rightarrow \alpha''$ transformation.

The texture of the FZ and HAZ in the deformed alloy was measured by EBSD. The band contrast (EBSD pattern quality) map and respective IPFs for $\alpha''$ and $\beta$ phases are shown in Figs. 5(d) and (e), respectively. Most of the grains have their $\langle 302 \rangle_{\alpha''}$, $\langle 110 \rangle_{\alpha''}$ and $\langle 111 \rangle_{\beta}$ directions approximately aligned to the ND, unlike what was observed for the substrate (see the IPF of the deformed alloy in Fig. 2(a)). Five other randomly chosen regions of the HAZ were analyzed in the same way, and similar results were observed. This shows that, despite the short heating time, LSM is able to alter the texture of the deformed alloy, producing a change in texture similar to that produced with the recrystallization process (Comparing Fig. 5(e) with Fig. 3(b)). This behavior can be explained by the formation of variants during the $\beta \rightarrow \alpha''$ phase transformation. When the laser heats the surface, a region is heated above the $\beta$-transus temperature and the $\alpha''$ phase therefore transforms to $\beta$ phase. When cooled, this transforms back to $\alpha''$ phase, which has six variants with different orientations. In this case, the substrate initially has a $[302]_{\alpha''}$//ND texture component, which transforms to a $[111]_{\beta}$//ND component when heated above the $\beta$-transus, according to the OR between the $\alpha''$ and $\beta$ phases. When cooled, the $[111]_{\beta}$//ND texture will originate the $[302]_{\alpha''}$//ND and $[110]_{\alpha''}$//ND components since there are six possible variants of $\alpha''$ for each orientation of the parent $\beta$ phase, as explained in Section 3.1 (Fig. 4).

For the recrystallized alloy, no apparent change was observed in the HAZ, which had the same grain size and microstructure as the substrate (Figs. 6(a, b)). EBSD analysis of the FZ and HAZ showed that the texture components of the modified surface layer are the same as those of the substrate (recrystallized condition), as observed in the IPFs of $\alpha''$ and $\beta$ phases (Comparing Fig. 6(c) with Fig. 3(b)).

To reveal more details of the effects of LSM
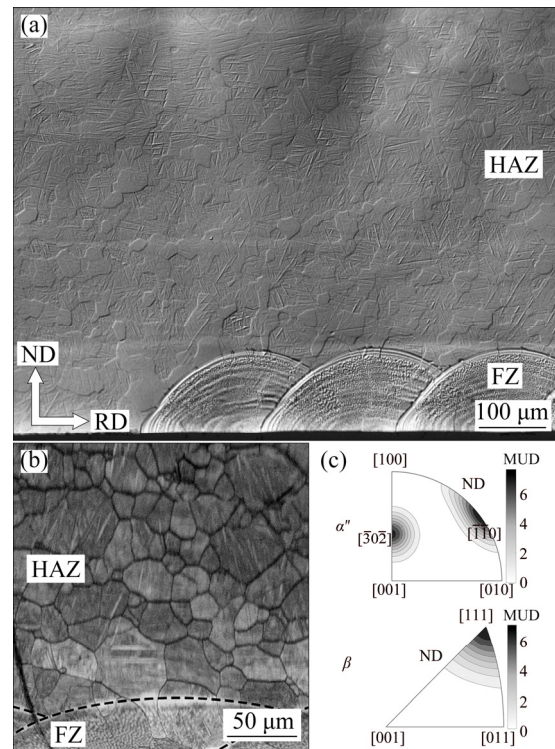


**Fig. 6** Microscopy analysis of recrystallized and laser-surface-melted sample (Dashed lines indicate FZ/HAZ interface): (a) VLM micrograph showing general view of FZ and HAZ; (b) EBSD band contrast map; (c) Inverse pole figures for $\alpha''$ and $\beta$ phases

on the microstructure and segregation of elements in the FZ, EBSD analysis was performed at higher magnification. Simultaneously, the energy-dispersive X-ray spectroscopy (EDS) mapping was carried out to determine whether Ti, Nb and Sn segregated during solidification. As the results for the deformed and recrystallized specimens were similar, only the analysis of the recrystallized alloy will be shown. The band contrast map (Fig. 7(a)) depicts the microstructure, and the IPF orientation maps for $\beta$ (Fig. 7(b)) and $\alpha''$ (Fig. 7(c)) phases show which crystal directions are aligned to the ND. The portion of the FZ that underwent planar solidification consists only of $\beta$ phase. In addition, evenly distributed $\beta$-phase "pools" surrounded by $\alpha''$ laths can be seen, where cellular solidification took place. The EDS maps for Ti, Nb and Sn (Figs. 7(d−f)) show that the regions only composed of $\beta$ phase are enriched with Nb and depleted of Ti. As Nb is a $\beta$-stabilizer element, it prevents the formation of $\alpha''$ phase during cooling. No apparent Sn segregation is observed in the EDS map, which can be explained by the low diffusivity of this
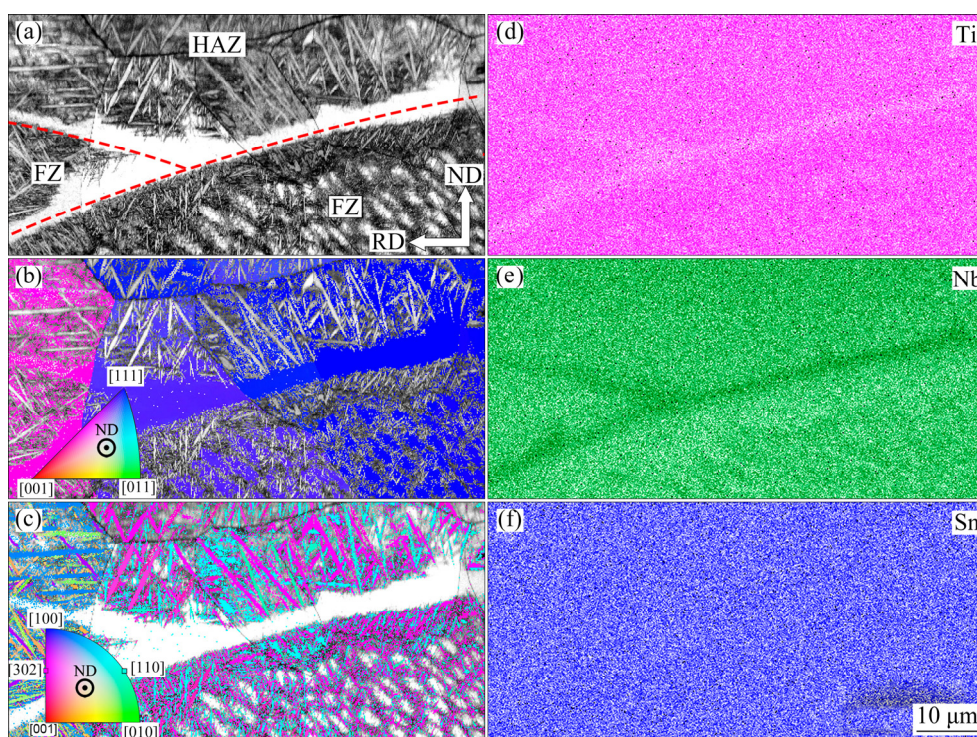
**Fig. 7** EBSD analysis of recrystallized and laser-surface-melted sample: (a) Band contrast (BC) map with FZ/HAZ interface marked with red dashed line; (b, c) Orientation maps for $\beta$ (b) and $\alpha''$ (c) phases superimposed on BC map; (d, e, f) EDS maps for Ti (d), Nb (e) and Sn (f)

element in Ti alloys [42]. Additionally, the IPF maps show that the crystal orientations of both phases ($\beta$ and $\alpha''$) are the same in the HAZ and FZ (Figs. 7(b) and (c), respectively), corroborating the epitaxial nature of the solidification already observed in Fig. 5(b) and indicating that the crystallographic orientation of the FZ follows that of the grains in the HAZ. Hence, LSM cannot change the crystallographic orientations of the grains in the FZ unless those of the grains in the HAZ are also changed.

### 3.3 Hardness and elastic modulus

The hardness and elastic modulus of the deformed alloy are about 3.1 and 63 GPa, respectively. After recrystallization, the hardness decreased to 2.5 GPa while the elastic modulus increased to 74 GPa. Measurements were performed in the ND−RD plane using instrumented indentation (nanoindentation). The higher hardness of the deformed alloy can be explained by the well-known strain-hardening effect, which is caused by the increase in dislocation density after cold working. Since the number of defects is greatly reduced during recrystallization, the hardness of the

recrystallized alloy is lower than that of the deformed alloy. The decrease in elastic modulus with cold deformation, in turn, has already been reported in other studies on Ti alloys. LI et al [43] attributed the reduction in the elastic modulus of commercially pure titanium alloy after severe deformation to the increase in lattice defects and grain boundaries, which weaken the bonding between atoms. The correlation between elastic modulus and dislocations was firstly discussed by MOTT [44]. Later, SAITO [45] reported significant reductions in elastic modulus after cold deformation in certain Ti alloys, such as Ti−23Nb−0.7Ta−2Zr−1.2O (at.%); however, he attributed these reductions not to dislocations but to the presence of "giant faults" that originated during deformation.

The effect of LSM on the hardness and elastic modulus of the deformed and recrystallized alloys is shown in Fig. 8. The values are shown against the distance from the fusion zone and, in the case of the deformed and laser-surface-melted sample (Fig. 8(a)), exhibiting a clear gradient between the modified surface region and the substrate, the latter being harder and more flexible (i.e. it has a lower elastic modulus) than the thermally treated surface.

In the FZ, the hardness and elastic modulus are about 2.6 and 72 GPa, respectively. As the distance from the FZ increases, there is a gradual increase in hardness and decrease in elastic modulus until the values for the substrate are reached. This behavior can be explained by the fact that the effects of cold rolling are eliminated in the FZ and HAZ in proportion to the heat input, which is inversely proportional to the distance from the surface. The recrystallized and laser-surface-melted sample (Fig. 8(b)) did not show any significant difference in the property between different zones, and the scatter of the values was significantly greater for this sample than that for the deformed alloy.

The differences in properties between different zones can be related not only to the degree of deformation, but also to the crystallographic texture [46,47]. Nevertheless, although some studies have successfully demonstrated that nano-indentation measurements are sensitive to crystal orientation [48–50], this type of analysis is not straightforward. In nanoindentation tests the deformation imposed by the indenter is triaxial and dependent on the tip geometry. In addition,

depending on how refined the microstructure is, the affected volume under the indenter may contain more than one grain or phase, making the deformation during measurement more complex. To verify whether texture had some influence on the nanoindentation results in this study, nano-indentation measurements were performed over grains with a known orientation (determined by EBSD), as shown in Fig. 9. For clarity, only orientations of the $\beta$ matrix are shown (if the $\beta$-phase crystal orientations are similar, the $\alpha''$-phase orientations are also necessarily similar). It can be clearly seen that grains with different orientations have similar values of elastic modulus (Fig. 9(a)) and hardness (Fig. 9(b)). In other words, even though the nanoindentation results may have been affected by texture, no correlation was found.

Since LSM can cause changes in crystallographic texture similar to those produced by recrystallization, as shown in this study, this surface treatment could be used as an alternative method for changing the surface properties of alloys, such as corrosion resistance and biocompatibility [51].
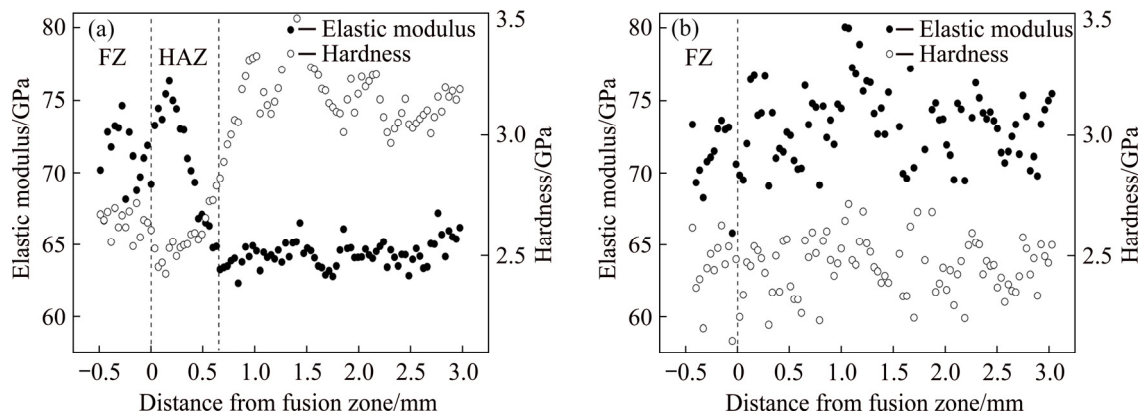


**Fig. 8** Nanoindentation measurements for deformed (a) and recrystallized (b) alloys subjected to LSM
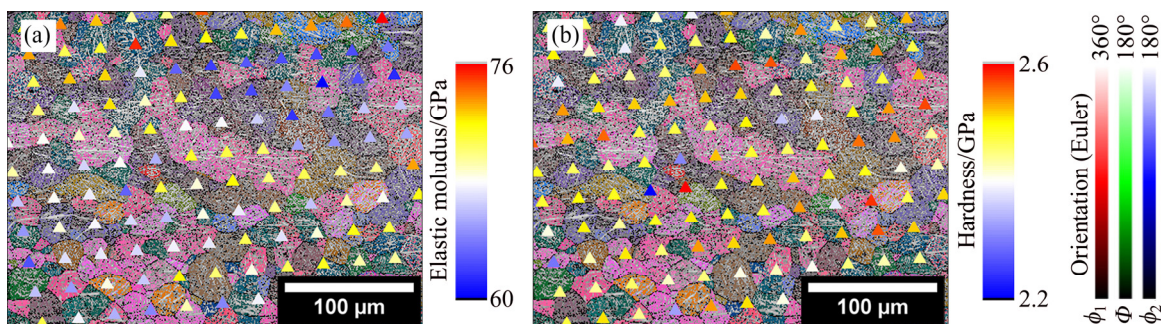


**Fig. 9** Correlation between $\beta$-grain orientation (colored EBSD Euler map) and elastic modulus (a) and hardness (b) as measured by nanoindentation (Locations of indentations are indicated by triangles colored according to respective values of elastic modulus and hardness)

The gradient in the elastic modulus observed here is a feature that has attracted the attention of researchers recently. As mentioned in the introduction, some studies have shown that femoral implants with a higher elastic modulus in the proximal region and lower modulus in the distal region can minimize some frequently observed problems, such as stress shielding and interface micromotions [6]. FOGAGNOLO et al [52,53], studying elastic modulus gradients between surface and substrate as a way of improving fatigue strength, obtained a stiffness-graded material with a surface layer of 30% less rigid than, and twice as hard as, the substrate by controlling the surface composition with a technique known as laser surface alloying. They suggested that a more flexible coating should be able to increase fatigue strength by lowering tensile stresses on the surface, where most fatigue cracks usually start. In the present work, in which previously deformed Ti−30Nb−4Sn alloy was subjected to LSM, the stiffness gradient obtained was the opposite of that reported by FOGAGNOLO et al [52,53], i.e., the surface layer was stiffer than the substrate. Higher rigidity on the surface may be advantageous for implants as it should decrease the effect of micromotions at the implant/bone interface. Further studies are required to determine, in practice, the effects of surface−substrate stiffness gradients on the biomechanical behavior of implants.

## 4 Conclusions

(1) XRD texture analysis of the $\alpha''$ phase showed that the main texture components of the deformed alloy were the $[302]_{\alpha''}$//ND fiber with its maximum at $(101)[0\bar{1}0]$. After recrystallization, the $[302]_{\alpha''}$//ND fiber was still present but with a stronger intensity, and a new component, $[110]_{\alpha''}$//ND, appeared.

(2) Although the $\beta$-phase texture could not be measured by XRD, it was successfully predicted for the recrystallized alloy ($[111]_{\beta}$//ND) by considering the orientation relationship of which the $\alpha''$ and $\beta$ phases must obey. This texture component was confirmed by EBSD analysis.

(3) The elastic modulus of the Ti−30Nb−4Sn alloy decreased after cold rolling.

(4) LSM of the deformed alloy produced changes in the texture of the surface layer affected by the heat from the laser (FZ and HAZ) similar to those produced by recrystallization.

(5) LSM produced a surface layer with a higher elastic modulus and lower hardness on the previously deformed alloy but produced no change in the surface layer in the case of the recrystallized alloy.

## References

[1] NIINOMI M, LIU Y, NAKAI M, LIU H H, LI H. Biomedical titanium alloys with Young's moduli close to that of cortical bone [J]. Regenerative Biomaterials, 2016, 3: 173−185.

[2] MURPHY W L, BLACK J, HASTINGS G W. Handbook of biomaterial properties [M]. Boston, MA: Springer, 1998.

[3] de VITERI V S, FUENTES E. Titanium and titanium alloys as biomaterials [M]. New York: InTech, 2013.

[4] SIMÕES J A, MARQUES A T. Design of a composite hip femoral prosthesis [J]. Materials and Design, 2005, 26: 391−401.

[5] LOPES E S N, CONTIERI R J, BUTTON S T, CARAM R. Femoral hip stem prosthesis made of graded elastic modulus metastable $\beta$ Ti Alloy [J]. Materials & Design, 2015, 69: 30−36.

[6] SIMÕES J A, MARQUES A T, JERONIMIDIS G. Design of a controlled-stiffness composite proximal femoral prosthesis [J]. Composites Science and Technology, 2000, 60(4): 559−567.

[7] MILLER P D, HOLLADAY J W. Friction and wear properties of titanium [J]. Wear, 1958, 2(2): 133−140.

[8] LIU X Y, CHU P K, DING C X. Surface modification of titanium, titanium alloys, and related materials for biomedical applications [J]. Materials Science and Engineering R: Reports, 2004, 47: 49−121.

[9] BALLA V K, SODERLIND J, BOSE S, BANDYOPADHYAY A. Microstructure, mechanical and wear properties of laser surface melted Ti6Al4V alloy [J]. Journal of the Mechanical Behavior of Biomedical Materials, 2014, 32: 335−344.

[10] PRODANOV L, LAMERS E, WALBOOMERS X F, JANSEN J A. Initial cellular response to laser surface engineered biomaterials [J]. MRS Bulletin, 2011, 36: 1034−1042.

[11] SUWAS S, RAY R K. Crystallographic texture of materials [M]. London: Springer, 2014.

[12] BAHL S, SUWAS S, CHATTERJEE K. The importance of crystallographic texture in the use of titanium as an orthopedic biomaterial [J]. RSC Advances, 2014, 4: 38078.

[13] HAGIHARA K, OKUBO M, YAMASAKI M, NAKANO T. Crystal-orientation-dependent corrosion behaviour of single crystals of a pure Mg and Mg−Al and Mg−Cu solid solutions [J]. Corrosion Science, 2016, 109: 68−85.

[14] CUI Wen-fang, GUO Ai-hong, ZHOU Lian, LIU Chun-ming. Crystal orientation dependence of Young's modulus in Ti−Nb-based $\beta$-titanium alloy [J]. Science China Technological Sciences, 2010, 53: 1513−1519.

[15] ZHANG Ling-bo, WANG Ke-zheng, XU Li-juan, XIAO Shu-long, CHEN Yu-yong. Effect of Nb addition on microstructure, mechanical properties and castability of $\beta$-type Ti−Mo alloys [J]. Transactions of Nonferrous Metals Society of China, 2015, 25: 2214−2220.

[16] IBRAHIM M K, HAMZAH E, SAUD S N, NAZIM E M, BAHADOR A. Parameter optimization of microwave sintering porous Ti−23%Nb shape memory alloys for biomedical applications [J]. Transactions of Nonferrous Metals Society of China, 2018, 28: 700−710.

[17] FANTON L, de LIMA N B, de OLIVEIRA FRANÇA HAYAMA A, CARAM R, FOGAGNOLO J B. Texture development in cold deformed and recrystallized Ti−30Nb−4Sn alloy and its effects on hardness and Young's modulus [J]. Advanced Engineering Materials, 2017, 19: 1−6.

[18] SALVADOR C A F, OPINI V C, LOPES E S N, CARAM R. Microstructure evolution of Ti−30Nb−(4Sn) alloys during classical and step-quench aging heat treatments [J]. Materials Science and Technology, 2017, 33: 400−407.

[19] GAO J H, HUANG Y H, GUAN D K, KNOWLES A J, MA Le, DYE D, RAINFORTH W M. Deformation mechanisms in a metastable beta titanium twinning induced plasticity alloy with high yield strength and high strain hardening rate [J]. Acta Materialia, 2018, 152: 301−314.

[20] WANG Li-qiang, LU Wei-jie, QIN Ji-ning, ZHANG Fan, ZHANG Di. Microstructure and mechanical properties of cold-rolled TiNbTaZr biomedical beta titanium alloy [J]. Materials Science and Engineering A, 2008, 490: 421−426.

[21] XU Y F, YI D Q, LIU H Q, WU X Y, WANG B, YANG F L. Effects of cold deformation on microstructure, texture evolution and mechanical properties of Ti−Nb−Ta−Zr−Fe alloy for biomedical applications [J]. Materials Science and Engineering A, 2012, 547: 64−71.

[22] LEE C M, JU C P, CHERN LIN J H, LIN J H C, CHERN LIN J H. Structure−property relationship of cast Ti−Nb alloys [J]. Journal of Oral Rehabilitation, 2002, 29(4): 314−322.

[23] GEPREEL M A H. Texturing tendency in $\beta$-type Ti-alloys [M]. New York: InTech, 2013.

[24] LEE H P, ESLING C, BUNGE H J. Development of the rolling texture in titanium [J]. Textures and Microstructures, 1988, 7: 317−337.

[25] LIU N, WANG Y, HE W J, LI J, CHAPUIS A, LUAN B F, LIU Q. Microstructure and textural evolution during cold rolling and annealing of commercially pure titanium sheet [J]. Transactions of Nonferrous Metals Society of China, 2018, 28:1123−1131.

[26] LIU Ding-kai, HUANG Guang-sheng, GONG Gui-lin, WANG Guan-gang, PAN Fu-sheng. Influence of different rolling routes on mechanical anisotropy and formability of commercially pure titanium sheet [J]. Transactions of Nonferrous Metals Society of China, 2017, 27: 1306−1312.

[27] HU Ming, DONG Li-min, ZHANG Zhi-qiang, LEI Xiao-fei, YANG Rui, SHA Yu-hui. Effects of multi-pass drawing strain and heat treatment on microstructure, texture and mechanical properties of Ti−6Al−4V alloy [J]. Materials Science and Engineering A, 2019, 757: 70−83.

[28] ZHANG Yu, WANG Xiao-peng, KONG Fan-tao, SUN Liang-liang, CHEN Yu-yong. Microstructure, texture and mechanical properties of Ti−43Al−9V−0.2Y alloy hot-rolled at various temperatures [J]. Journal of Alloys and Compounds, 2019, 777: 795−805.

[29] ZHANG Jun-song, HAO Shi-jie, JIANG Da-qiang, HUANG Yong, CUI Li-shan, LIU Yi-nong, YANG Hong, REN Yang. In situ synchrotron high-energy X-ray diffraction study of microscopic deformation behavior of a hard-soft dual phase composite containing phase transforming matrix [J]. Acta Materialia, 2017, 130: 297−309.

[30] HAY J, AGEE P, HERBERT E. Continuous stiffness measurement during instrumented indentation testing [J]. Experimental Techniques, 2010, 34: 86−94.

[31] BACHMANN F, HIELSCHER R, SCHAEBEN H. Texture analysis with MTEX-free and open source software toolbox [J]. Solid State Phenomena, 2010, 160: 63−68.

[32] HIELSCHER R, SCHAEBEN H. A novel pole figure inversion method: Specification of the MTEX algorithm [J]. Journal of Applied Crystallography, 2008, 41: 1024−1037.

[33] KIM H Y, IKEHARA Y, KIM J I, HOSODA H, MIYAZAKI S. Martensitic transformation, shape memory effect and superelasticity of Ti−Nb binary alloys [J]. Acta Materialia, 2006, 54(9): 2419−2429.

[34] BERTRAND E, CASTANY P, GLORIANT T. An alternative way to orient the parent phase in the cubic/orthorhombic martensitic transformation of titanium shape memory alloys [J]. Scripta Materialia, 2014, 83: 41−44.

[35] HIELSCHER R. MTEX toolbox [EB/OL]. [2019-11-13]. https://mtex-toolbox. github.io/.

[36] HUMPHREYS F. Characterisation of fine-scale micro-structures by electron backscatter diffraction (EBSD) [J]. Scripta Materialia, 2004, 51(8): 771−776.

[37] HAYAMA A O F, LOPES J F S C, GOMES DA SILVA M J, ABREU H F G, CARAM R. Crystallographic texture evolution in Ti−35Nb alloy deformed by cold rolling [J]. Materials and Design, 2014, 60: 653−660.

[38] MATSUMOTO H, WATANABE S, HANADA S. Beta TiNbSn alloys with low Young's modulus and high strength [J]. Materials Transactions, 2005, 46: 1070−1078.

[39] MATSUMOTO H, WATANABE S, HANADA S. Microstructures and mechanical properties of metastable $\beta$ TiNbSn alloys cold rolled and heat treated [J]. Journal of Alloys and Compounds, 2007, 439: 146−155.

[40] NYUNG D, NAM H. Recrystallization textures of metals and alloys [M]. New York: InTech, 2013.

[41] KURZ W, FISHER D J. Fundamentals of solidification [M]. Aedermannsdorf, Switzerland: Trans Tech Publications, 1998.

[42] DAL BÓ M R, SALVADOR C A F, MELLO M G, LIMA D D, FARIA G A, RAMIREZ A J, CARAM R. The effect of Zr and Sn additions on the microstructure of Ti−Nb−Fe gum metals with high elastic admissible strain [J]. Materials and Design, 2018, 160: 1186−1195.

[43] LI Zhi-ming, FU Li-ming, FU Bin, YANG Xiao-ping, SHAN Ai-dang. Nanoindentation hardness and elastic modulus of nano-grained titanium produced by asymmetric and symmetric rolling [J]. Journal of Nanoscience and Nanotechnology, 2014, 14: 7740−7744.

[44] MOTT N F. CXVII. A theory of work-hardening of metal crystals [J]. The London, Edinburgh, and Dublin Philosophical Magazine and Journal of Science, 1952, 43: 1151−1178.

[45] SAITO T. Multifunctional alloys obtained via a dislocation-free plastic deformation mechanism [J]. Science, 2003, 300: 464−467.

[46] PANIGRAHI A, SULKOWSKI B, WAITZ T, OZALTIN K, CHROMINSKI W, PUKENAS A, HORKY J, LEWAN-DOWSKA M, SKROTZKI W, ZEHETBAUER M. Mechanical properties, structural and texture evolution of biocompatible Ti−45Nb alloy processed by severe plastic deformation [J]. Journal of the Mechanical Behavior of Biomedical Materials, 2016, 62: 93−105.

[47] HANADA S, MASAHASHI N, JUNG T K, YAMADA N, YAMAKO G, ITOI E. Fabrication of a high-performance hip prosthetic stem using $\beta$ Ti−33.6Nb−4Sn [J]. Journal of the Mechanical Behavior of Biomedical Materials, 2014, 30: 140−149.

[48] WANG W C, LU K. Nanoindentation measurement of hardness and modulus anisotropy in $Ni_3Al$ single crystals [J]. Journal of Materials Research, 2002, 17: 2314−2320.

[49] HAUŠILD P, MATERNA A, NOHAVA J. Characterization of anisotropy in hardness and indentation modulus by nanoindentation [J]. Metallography, Microstructure, and Analysis, 2014, 3(1): 5−10.

[50] RENNER E, GAILLARD Y, RICHARD F, AMIOT F, DELOBELLE P. Sensitivity of the residual topography to single crystal plasticity parameters in Berkovich nanoindentation on FCC nickel [J]. International Journal of Plasticity, 2016, 77: 118−140.

[51] HOSEINI M, BOCHER P, SHAHRYARI A, AZARI F, SZPUNAR J A, VALI H. On the importance of crystallographic texture in the biocompatibility of titanium based substrate [J]. Journal of Biomedical Materials Research: Part A, 2014, 102: 3631−3638.

[52] FOGAGNOLO J B, RODRIGUES A V, SALLICA-LEVA E, LIMA M S F, CARAM R. Surface stiffness gradient in Ti parts obtained by laser surface alloying with Cu and Nb [J]. Surface and Coatings Technology, 2016, 297: 34−42.

[53] FOGAGNOLO J B, RODRIGUES A V, LIMA M S F, AMIGÓ V, CARAM R. A novel proposal to manipulate the properties of titanium parts by laser surface alloying [J]. Scripta Materialia, 2013, 68: 471−474.

# 激光表面熔化对 Ti−30Nb−4Sn 合金晶体织构、显微组织、弹性模量和硬度的影响

Leonardo FANTON[1], Nelson Batista de LIMA[2], Emilio Rayón ENCINAS[3],
Vicente Amigó BORRÁS[3], Conrado Ramos Moreira AFONSO[4], João Batista FOGAGNOLO[1]

1. School of Mechanical Engineering, University of Campinas, Rua Mendeleyev, 200, CEP 13083-860, Campinas, SP, Brazil;
2. Instituto de Pesquisas Energéticas e Nucleares, Av. Prof. Lineu Prestes, 2242, CEP 05508-000, São Paulo, SP, Brazil;
3. Institut de Tecnologia de Materials, Universitat Politècnica de València,
Camino de Vera, s/n, Código Postal 46022, Valencia, Spain;
4. Department of Materials Engineering, Federal University of São Carlos,
Rodovia Washington Luís, Km 235, CEP 13565-905, São Carlos, SP, Brazil

摘　要：骨科植入物的生物相容性与其弹性模量和表面性能密切相关。本研究的目的是阐明冷轧、再结晶和表面激光熔化(LSM)对双相$(\alpha''+\beta)$Ti−30Nb−4Sn 合金显微组织和力学性能的影响。对冷轧态基体进行 X 射线衍射织构分析(XRD)显示有$[302]_{\alpha''}//ND$ 织构成分，而对再结晶态基体的分析显示有$[302]_{\alpha''}//ND$ 和$[110]_{\alpha''}//ND$ 织构成分。XRD 不能直接检测出 $\beta$ 相织构，但是通过考虑 $\alpha''$相和 $\beta$ 相之间的位向关系可成功预测出$[111]_{\beta}||ND$ 织构的存在。纳米压痕测试结果表明，冷轧态基体的弹性模量(63 GPa)低于再结晶态基体(74 GPa)。根据已有文献和本文研究结果，认为这种差异是由冷变形过程中晶体缺陷的引入造成的。纳米压痕/EBSD 分析表明，纳米压痕结果不受晶体取向的影响。LSM 对变形合金硬度、弹性模量和晶体织构产生的变化类似于再结晶热处理产生的变化，均在表面和基体之间产生刚度梯度。

关键词：钛合金；冷轧；激光表面熔化；再结晶；晶体织构；刚度梯度材料

**(Edited by Wei-ping CHEN)**